Distribution of cholinergic nerve terminals in the aged human brain measured with [18F]FEOBV PET and its correlation with histological data

Okkels, Niels; Horsager, Jacob; Labrador-Espinosa, Miguel A.; Hansen, Frederik O.; Andersen, Katrine B.; Just, Mie Kristine; Fedorova, Tatyana D.; Skjærbæk, Casper; Munk, Ole L.; Hansen, Kim V.; Gottrup, Hanne; Hansen, Allan K.; Grothe, Michel J.; Borghammer, Per

Published in:
NeuroImage

DOI (link to publication from Publisher):
10.1016/j.neuroimage.2023.119908

Publication date:
2023

Document Version
Publisher's PDF, also known as Version of record

NeuroImage 269 (2023) 119908

Contents lists available at ScienceDirect

NeuroImage

journal homepage: www.elsevier.com/locate/neuroimage

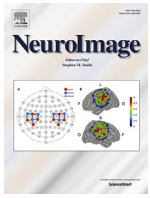

Distribution of cholinergic nerve terminals in the aged human brain measured with [^{18}F]FEOBV PET and its correlation with histological data

Niels Okkels[a,b,c,*], Jacob Horsager[a], Miguel A. Labrador-Espinosa[d,e], Frederik O. Hansen[a,b], Katrine B. Andersen[a,b], Mie Kristine Just[a,b], Tatyana D. Fedorova[a,b], Casper Skjærbæk[a,b], Ole L. Munk[a,b], Kim V. Hansen[a], Hanne Gottrup[c], Allan K. Hansen[a,f], Michel J. Grothe[d,e,1], Per Borghammer[a,1]

[a] Department of Nuclear Medicine and PET, Aarhus University Hospital, Aarhus, Denmark
[b] Department of Clinical Medicine, Aarhus University, Aarhus, Denmark
[c] Department of Neurology, Aarhus University Hospital, Aarhus, Denmark
[d] Unidad de Trastornos del Movimiento, Servicio de Neurología y Neurofisiología Clínica, Instituto de Biomedicina de Sevilla (IBiS), Hospital Universitario Virgen del Rocío/CSIC/Universidad de Sevilla, Seville, Spain
[e] Centro de Investigación Biomédica en Red Sobre Enfermedades Neurodegenerativas (CIBERNED), Instituto de Salud Carlos III, Madrid, Spain
[f] Department of Nuclear Medicine, Aalborg University Hospital, Aalborg, Denmark

ARTICLE INFO

Keywords:
Brain
Cholinergic Neurons
VAChT Proteins
PET-CT
mRNA
Healthy Volunteer

ABSTRACT

Introduction: [^{18}F]fluoroetoxybenzovesamicol ([^{18}F]FEOBV) is a positron emission topography (PET) tracer for the vesicular acetylcholine transporter (VAChT), a protein located predominantly in synaptic vesicles in cholinergic nerve terminals. We aimed to use [^{18}F]FEOBV PET to study the cholinergic topography of the healthy human brain.

Materials and methods: [^{18}F]FEOBV PET brain data volumes of healthy elderly humans were normalized to standard space and intensity-normalized to the white matter. Stereotactic atlases of regions of interest were superimposed to describe and quantify tracer distribution. The spatial distribution of [^{18}F]FEOBV PET uptake was compared with histological and gene expression data.

Results: Twenty participants of both sexes and a mean age of 73.9 ± 6.0 years, age-range [64; 86], were recruited. Highest tracer binding was present in the striatum, some thalamic nuclei, and the basal forebrain. Intermediate binding was found in most nuclei of the brainstem, thalamus, and hypothalamus; the vermis and flocculonodular lobe; and the hippocampus, amygdala, insula, cingulate, olfactory cortex, and Heschl's gyrus. Lowest binding was present in most areas of the cerebral cortex, and in the cerebellar nuclei and hemispheres. The spatial distribution of tracer correlated with immunohistochemical post-mortem data, as well as with regional expression levels of *SLC18A3*, the VAChT coding gene.

Discussion: Our *in vivo* findings confirm the regional cholinergic distribution in specific brain structures as described post-mortem. A positive spatial correlation between tracer distribution and regional gene expression levels further corroborates [^{18}F]FEOBV PET as a validated tool for *in vivo* cholinergic imaging. The study represents an advancement in the continued efforts to delineate the spatial topography of the human cholinergic system *in vivo*.

1. Introduction

Cholinergic neurons, which produce and release the neurotransmitter acetylcholine, are distributed throughout the human brain, and play a key role in various functions such as motor control, autonomic regulation, and cognition (Oda, 1999). In the brainstem, cholinergic neurons in the parasympathetic nuclei project axons to smooth muscles in glands and organs, while those in the somatic motor nuclei project to striated muscles in the face, neck, and tongue. Cholinergic cell groups in the reticular formation and basal forebrain have axons that project to other brain regions including the cortex, limbic system, thalamus, and hypothalamus.

[^{18}F]Fluoroetoxybenzovesamical ([^{18}F]FEOBV) is a positron emission topography (PET) radioligand for the vesicular acetylcholine trans-

* Corresponding author at: Department of Nuclear Medicine and PET, Aarhus University Hospital, Palle Juul-Jensens Boulevard 165, J220, Aarhus N 8200, Denmark
E-mail address: niels.okkels@clin.au.dk (N. Okkels).
[1] These authors contributed equally as senior authors.

https://doi.org/10.1016/j.neuroimage.2023.119908.
Received 2 December 2022; Received in revised form 10 January 2023; Accepted 27 January 2023
Available online 29 January 2023.

porter (VAChT), the protein responsible for loading acetylcholine into presynaptic vesicles of cholinergic terminals. In the brain, VAChT is expressed uniquely in cholinergic neurons (Gilmor et al., 1996). This makes [^{18}F]FEOBV a very specific marker of the cholinergic neuronal phenotype. The cortical distribution of cholinergic terminals has previously been described in human *in vivo* studies using [^{18}F]FEOBV PET or [^{123}I]IBVM, a single-photon emission computerized tomography ligand for VAChT (Petrou et al., 2014; Kuhl et al., 1994; Albin et al., 2018). So far, the subcortical distribution of cholinergic terminals has received less attention.

Post-mortem studies have demonstrated a characteristic topographic distribution of cholinergic cell bodies and axons in several subcortical structures including the thalamus (Heckers et al., 1992), hypothalamus (Rao et al., 1987), and cerebellum (de Lacalle et al., 1993). Collectively, post-mortem evidence implies a specific role of cholinergic neurons that may be important to understand the function of these structures, such as pituitary function (Tago et al., 1987), sleep (Heckers et al., 1992), gait, and vestibular function (Barmack et al., 1992a). For these reasons, there could be several interesting prospects of advancing the methods used to explore the *in vivo* cholinergic anatomy of subcortical structures.

As such, delineating the detailed molecular anatomy of the cholinergic system is important to understand physiological processes of the healthy human brain, as well as pathological mechanisms involved in neurodegenerative, dysautonomic, and neuromuscular diseases. Therefore, in this study we use comprehensive regional analyses of [^{18}F]FEOBV PET binding to explore the distribution of cholinergic terminals in the human brain with a focus on subcortical regions. Also, the distribution of [^{18}F]FEOBV PET is compared to histological data from post-mortem studies. Finally, we assess the spatial correspondence of regional [^{18}F]FEOBV PET binding with the regional expression of *SLC18A3* messenger ribonucleic acid (mRNA), a measure of VAChT on the transcriptional level.

2. Materials and methods

2.1. Participants and setting

Aged subjects without neurological or psychiatric disease were recruited through advertisement in local newspapers for magnetic resonance imaging (MRI), positron emission topography (PET) with computed tomography (CT), and clinical examinations. Details of the cognitive assessment are presented in the Supplementary. All examinations were performed at the Department of Nuclear Medicine and PET, Aarhus University Hospital, Aarhus, Denmark. The study was conducted according to the Declaration of Helsinki and approved by the Central Denmark Region Committee on Health Research Ethics. All participants signed an informed consent form.

2.2. Imaging

PET/CT examinations were performed on a Siemens Biograph Vision 600 PET/CT camera (*Siemens Healthcare, Erlangen, Germany*). A 30-min PET acquisition was started 180 min after injection of ~200 MBq [^{18}F]FEOBV. A CT scan was performed prior to the PET recording for attenuation correction. Participants abstained from smoking for at least 5.5 h before PET acquisition. T1-MPRAGE sequences were obtained on a 3T Siemens Magnetom Skyra scanner and used for coregistration.

2.3. Data processing

First, the raw data was binned into six frames of five minutes and reconstructed using resolution recovery and time-of-flight (TrueX+TOF), 8 iterations, 5 subsets, 440 matrix, zoom 2, no filter, with final voxel size of 0.83 × 0.83 × 1.65 mm^3, and a spatial resolution of 2 mm full-width half-maximum (FWHM). Motion corrected PET image volumes were coregistered to the T1 images. The T1 images were segmented and spatially normalized to common MNI space (MNI152NLin2009cAsym template in SPM12) using high-dimensional spatial registration implemented in the DARTEL algorithm (Ashburner, 2007). The PET images were normalized by applying the deformation fields from the normalization of the T1 images, resulting in a final voxel-size of 1.5 mm^3 isotropic in the normalized PET images. The PET images were divided by decay corrected dose and body weight to calculate standard uptake values (SUV). The SUV values were then divided by the SUV of the centrum semiovale to yield SUV ratios (SUVR) (Aghourian et al., 2017). This late static approach has been shown to correlate highly with distribution volume ratios obtained from dynamic modelling (Petrou et al., 2014). Anatomical MNI-space atlases were then applied to the PET images to quantify regional differences in tracer uptake. Specifically, we used the Mori whole brain white matter atlas (Oishi et al., 2009); the Jülich Brain cytoarchitectonic atlas (Amunts et al., 2020); Hammers atlas (Hammers et al., 2003); SUIT probabilistic cerebellar atlas (Diedrichsen et al., 2009); relevant atlas from the Brainstem Navigator toolkit (Singh et al., 2019; García-Gomar et al., 2021; Bianciardi et al., 2018); atlas of thalamic nuclei (Saranathan et al., 2021); Yeo's atlas of cortical networks (Yeo et al., 2011); atlas of hypothalamic structures (Neudorfer et al., 2020); the automated anatomical atlas, third version (Rolls et al., 2020); an atlas of the olfactory cortex (Fjaeldstad et al., 2017); anterior and posterior regions of the basal forebrain (Fritz et al., 2019); and hippocampus (Wolf et al., 2017).

2.4. Comparison of regional [^{18}F]FEOBV PET signal distribution to histologic data and gene expression measurements

Brainstem images were angled perpendicular to the pontomesenchaphalic junction and the location of brainstem atlases and distribution of [^{18}F]FEOBV PET uptake was evaluated against a human histological brainstem atlas with similar orientation of slices (Coulombe et al., 2021). We used spatial correlation analyses using Spearman's rank correlations to compare the regional distribution of [^{18}F]FEOBV PET uptake to the regional distribution of enzymatic activity of choline acetyltransferase (ChAT) or acetylcholinesterase (AChE), or immunohistochemical ChAT in nerve fibers as described by published post-mortem studies (Heckers et al., 1992; Rao et al., 1987; de Lacalle et al., 1993; Davies and Maloney, 1976; DeKosky et al., 2002; Mesulam et al., 1992a, 1992b). The post-mortem histological studies were identified as follows: The literature was searched for studies reporting ChAT or AChE enzymatic activity, or ChAT staining intensity, in brain tissue. Priority was given to studies reporting findings on human over non-human species, elderly over younger, and healthy over diseased. The anatomical areas analysed in the different studies were matched to corresponding regions in the MNI-space atlases and a minimum of five regional matches was selected as an inclusion criterion for the correlational analysis. The categories of the semi-quantitative ordinal scales are reported as they appeared in the referenced histological studies.

For spatial correlation analyses with regional gene expression values, voxel-wise maps of predicted mRNA expression of relevant genes were downloaded from http://www.meduniwien.ac.at/neuroimaging/mRNA.html (Gryglewski et al., 2018). These included three genes for which we expected positive correlations: *SLC18A3*, the gene for VAChT; *CHAT*, the gene for cholineacetyltransferase; and *ACHE*, the gene for acetylcholinesterase. Also, we identified three non-cholinergic negative control genes for which we did not expect to see comparable spatial correlations with [^{18}F]FEOBV PET signal. These were *SV2A*, the gene for synaptic vesicle glycoprotein 2A; *SLC18A2*, the gene for vesicular monoamine transporter 2; and *SNCA*, the gene for alpha synuclein. In brief, the voxel-wise gene expression maps pool the full information of regional microarray-based mRNA expression measurements provided by the Allen Human Brain Atlas (including 3702 regional brain tissue samples derived from six brain donors: www.human.brain-map.org) (Hawrylycz et al., 2012). mRNA expression at locations without samples

was predicted using Gaussian process regression (Gryglewski et al., 2018). In our spatial correlation analyses, we compared the cerebral distribution of mRNA expression to that of the group average [^{18}F]FEOBV PET signal across 16 different cortical and subcortical brain regions as defined in the Hammers anatomical brain atlas.

2.5. Associations of regional [^{18}F]FEOBV PET signal with age

Finally, correlations between age and regional [^{18}F]FEOBV PET uptake were explored in subregions of the cerebral cortex, striatum, thalamus, hypothalamus, brainstem, and cerebellum. Correlations with a p-value < 0.05, false discovery rate (FDR) corrected, were considered significant. We conducted voxel-wise two-sample t-tests to compare the regional tracer uptake between non-smokers and current or previous smokers. In addition, we performed voxel-wise regression analyses of the effect of age on regional tracer uptake. Voxel-wise analyses were performed with a voxel-level height threshold of $p < .05$, FDR corrected, and a minimum cluster size of 50 voxels. Distribution of data was explored with histograms and Q-Q plots. Correlations were performed using Spearman's rank correlation or Pearson correlation as appropriate. PMOD was used for motion correction and calculating SUV. The CAT12 toolbox in SPM12 was used for imaging analyses and GraphPad Prism 9 for statistical analyses. Descriptive statistics are provided as mean±standard deviation or median (IQR).

3. Results

3.1. Participants

Twenty-six elderly participants were initially included. Of these, six were subsequently excluded for the following reasons: Structural abnormalities on MRI scan ($n = 2$), subjective cognitive complaints and MoCA < 24 ($n = 2$), and bradykinesia with rigidity on motor examination ($n = 2$). Thus, 20 participants were available for analyses. Participants were 74 ± 6 years of age, age-range [64;86], 13/20 (65%) male, 2/20 (10%] current smokers, and 10/20 (50%) previous smokers. At the time of their participation in the study, none of the participants were taking cholinergic, anticholinergic, or medications with cholinergic side effects. Two patients were taking medications that can cross the blood-brain barrier: chlorzoxazone and hydroxycarbamide. A comprehensive list of the medications taken by participants is provided in the Supplementary material. The median MoCA score was 28 (2.0).

3.2. Regional distribution of [^{18}F]FEOBV PET signal

Highest tracer binding was present in the putamen, caudate, and accumbens; the centromedian, lateral geniculate, and mediodorsal nucleus of the thalamus; and the basal forebrain. Intermediate binding was found in most investigated nuclei of the brainstem, thalamus, and hypothalamus; the vermis and flocculonodular lobe of the cerebellum; as well as key limbic circuit structures such as the hippocampus, amygdala, insula, cingulate, and olfactory cortex. Lowest binding was present in the cerebellar nuclei and hemispheres, and in most non-limbic areas of the cerebral cortex (Table 1). The general distribution of [^{18}F]FEOBV PET uptake is presented in Figs. 1 and 2.

The average SUVR of [^{18}F]FEOBV PET was 1.64 ± 0.17 in the cerebral cortex, 1.90 ± 0.16 in the brainstem, 1.86 ± 0.35 in the cerebellum, 2.68 ± 0.30 in the hypothalamus, 3.08 ± 0.39 in the thalamus, and 9.41 ± 1.29 in the striatum (mean±SD). Overall, tracer binding was significantly higher in all major subcortical regions compared to the cerebral cortex (paired t-tests, all $p < .01$).

Visual inspection of our images with a focus on the cerebral cortex revealed clear and distinct signals confined to the location of the olfactory cortex, Heschl's gyrus, anterior cingulate, insula, amygdala, hippocampus, and primary motor cortex (Figs. 1 and 2). These differences in intra-cortical signal distribution were confirmed using signal quantification within standardized atlas-based definitions of these and other cortical regions (Table 1). The difference between the cortical network with lowest (visual network, 1.46 ± 0.18) versus highest (somatomotor network, 1.95 ± 0.25) average SUVR was significant (paired *t*-test, $p < .001$).

Visual assessment of the brainstem revealed a detailed and heterogeneous cholinergic innervation. Overall, the signal was most prominent in the medulla oblongata and mesencephalon. Throughout the brainstem, the signal was predominantly located close to the midline in the dorsal tegmentum, and more intense in the upper compared to the lower brainstem. In the mesencephalon, the uptake of tracer was predominantly aligned with the location of structures in the reticular formation (Fig. 3). These were the dorsal raphe, mesencephalic reticular formation, isthmic reticular formation, pedunculopontine nucleus, parabigeminal nucleus, and periaqueductal grey including the parasympathetic nucleus Edinger Westphal and somatic motor nuclei of the 3rd to 4th cranial nerves (Table 1). Also, there was high uptake in the cuneiform nucleus, which is considered a continuation of the reticular formation overlapping the pedunculopontine nucleus. In the rostral mesencephalon, there was a high uptake in the superior colliculus and a moderate uptake in the red nucleus.

In the pons there was high uptake in the pontine tegmentum corresponding to the nuclei of 5th, 6th, 7th, and 8th cranial nerve and the pontine reticular formation including the pontine reticular nuclei, paramedian reticular nucleus, and median raphe (Table 1). Furthermore, a signal was located corresponding to the locus coeruleus. On the pontomesencephalic junction there was an uptake in the dorsal midline bordering the fourth ventricle, corresponding to the location of the caudal sectors of the laterodorsal tegmental nucleus and most caudal part of the pedunculopontine nucleus (Fig. 3, row c).

In the caudal medulla oblongata, the peak cholinergic uptake located to the midline corresponding to the visceromotoric dorsal motor nucleus of the vagus (DMV) and the somatomotoric hypoglossus nucleus (XII) (Fig. 4, b). In the rostral medulla the signal divided in two clearly separate columns, retaining the anatomical location of the DMV and XII (Fig. 3, rows d to f). On the pontomedullary junction the columnar signal increased corresponding to the location of the medial vestibular nucleus (MVN), and then tapered off in the caudal pons (Fig. 3, row d). This observation aligned with the known anatomical location of the vestibular nuclei complex as a rostral continuation of the DMV (Fig. 4a).

3.3. Correspondence of regional [^{18}F]FEOBV PET signal distribution to histologic data and gene expression measurements

The regional distribution of cholinergic enzyme activity and cholinergic immunohistochemical staining correlated spatially with the regional distribution of [^{18}F]FEOBV PET in approximately matched brain regions. The spatial correlations were found across studies using different methods and assessments across diverse anatomical systems. Six studies reported findings in post-mortem material from healthy humans using samples from the cerebral cortex, striatum, limbic areas, cerebellum, brainstem, and thalamus (Fig. 5, panels a - g). No eligible human studies investigating the hypothalamus were identified. Instead, one study on the rat hypothalamus was included (Fig. 5, panel h). All Spearman's rank correlations coefficients were positive in the range of $r_s = 0.62$ to 1 and statistically significant with p-values of 0.05 or smaller. Information on study subjects, methods for measuring enzymatic activity and staining, and sampled anatomical regions with matched MNI-space regions and atlases are presented in Supplementary Table 1. Using the "Robust regression and Outlier removal" (ROUT) method as implemented in GraphPad Prism 9, with a Q value of 1%, we identified the caudate nucleus as an outlier in two of the spatial association studies (Fig. 5, panels a and b). When we removed the

Table 1
Bilaterally averaged standard uptake value ratios (SUVR) of [^{18}F]FEOBV PET within selected regions of interest.

Region	SUVR	SD	Region	SUVR	SD	Region	SUVR	SD
Striatum			**Brainstem**			DMN	1.76	0.20
Putamen	10.7	1.55	CnF	3.76	0.43	FPN	1.74	0.20
Caudate	8.07	1.08	DR	3.66	0.48	DAN	1.61	0.19
Accumbens	7.23	0.95	PAG	3.54	0.42	Vis	1.46	0.18
Pallidum			isRt	3.52	0.33	**Olfactory cortex**		
	3.51	0.51	mRt	3.35	0.29		2.60	0.34
Thalamus			MnR	3.20	0.46	**Insula**		
CM	6.22	0.80	SC	3.07	0.47		2.55	0.31
LGN	5.39	1.07	VSM	3.00	0.31	**Heschl's gyrus**		
MD	4.10	0.69	PMnR	2.97	0.38	TE 1.1	2.12	0.37
MTT	3.28	0.33	RN	2.81	0.26	TE 1.0	2.10	0.37
VA	2.99	0.38	SubC	2.71	0.33	TE 1.2	1.93	0.32
VPL	2.95	0.39	PnO_PnC	2.69	0.30	**Cingulum**		
Pul	2.83	0.40	PTg	2.69	0.30	CGa	2.07	0.25
VLp	2.81	0.42	Rob	2.68	0.39	CGp	2.01	0.23
AV	2.75	0.47	sMRt	2.57	0.22	**Cerebellum**		
MGN	2.75	0.35	CLi_RLi	2.51	0.33	VIIb (vermis)	3.63	0.73
VLa	2.45	0.28	SOC	2.50	0.33	VIIIa (vermis)	3.45	0.70
Hb	1.88	0.53	RMg	2.45	0.30	IX (uvula)	3.41	0.57
Hypothalamus			Ve	2.39	0.32	VIIIb (vermis)	3.17	0.57
AHA	3.65	0.56	PCRtA	2.34	0.25	VI (vermis)	2.78	0.53
DM	3.41	0.54	LC	2.30	0.32	CrusII (vermis)	2.69	0.63
VM	3.26	0.44	iMRt	2.26	0.21	X (nodulus)	2.50	0.41
LH	3.20	0.35	LDTg_CGPn	2.17	0.32	X (flocculus)	2.49	0.40
MPO	3.16	0.51	MPB	2.14	0.27	IV (lobule)	2.49	0.41
pH	2.84	0.54	MiTg_PBG	2.05	0.24	V (lobule)	2.19	0.47
SO	2.61	0.47	SN2	2.03	0.14	Fastigial	2.35	0.32
TM	2.58	0.51	SN	2.00	0.15	VI (lobule)	1.90	0.40
BNST	2.43	0.29	SN1	1.98	0.17	Interposed	1.90	0.18
DPEH	2.42	0.52	LPB	1.69	0.22	IX (tonsil)	1.83	0.32
ITP	2.39	0.18	IC	1.52	0.26	VIIIa (lobule)	1.82	0.39
AN	2.26	0.45	RPa	1.38	0.17	VIIIb (lobule)	1.82	0.39
Pa	1.99	0.48	ION	1.15	0.15	VIIb (lobule)	1.80	0.42
SCh	1.81	0.39	**Cortical lobes**			CrusI (lobule)	1.71	0.35
MM	1.66	0.32	Frontal	1.71	0.18	CrusII (lobule)	1.71	0.40
Basal forebrain			Temporal	1.68	0.17	Dentate	1.67	0.13
aBF	4.59	0.65	Parietal	1.54	0.15	CrusI (vermis)	1.41	0.50
pBF	4.59	0.73	Occipital	1.45	0.16			
Hippocampus			**Cortical networks**					
	2.86	0.28	SM	1.95	0.25			
Amygdala			Sal/VA	1.94	0.24			
	3.26	0.38	Lim	1.89	0.20			

Twenty [^{18}F]FEOBV PET images of healthy elderly subjects were transferred to MNI-space and averaged. Stereotactic atlases were superimposed to define regions of interest and extract SUVR values. aBF, anterior basal forebrain; AHA, anterior hypothalamic area; AN, arcuate hypothalamic nucleus; AV, anteroventral nucleus; BNST, bed nucleus of the stria terminalis; CGa, anterior cingulate; CGp, posterior cingulate; CLi_RLi, caudal-rostral linear raphe; CM, centromedian nucleus; CnF, cuneiform nucleus; DAN, dorsal attention network; DMN, default mode network; DM, dorsomedial hypothalamic nucleus; DPEH, dorsal periventricular hypothalamic nucleus; DR, dorsal raphe; FPN, frontoparietal (control) network; Hb, habenula; IC, inferior colliculus; iMRt, inferior medullary reticular formation; ION, inferior olivary nucleus; isRt, isthmic reticular formation; ITP, inferior thalamic peduncle; LC, locus coeruleus; LDTg_CGPn, laterodorsal tegmental nucleus and central grey of the rhombencephalon; LGN, lateral geniculate nucleus; LH, lateral hypothalamus; Lim, limbic network; LPB, lateral parabrachial nucleus; MD, mediodorsal nucleus; MGN, medial geniculate nucleus; MiTg_PBG, microcellular tegmental nucleus – parabigeminal nucleus; MM, mammillary bodies; MnR, median raphe; MPB, medial parabrachial nucleus; MPO, medial preoptic nucleus; mRt, mesencephalic reticular formation; MTT, mammillothalamic tract; Pa, paraventricular nucleus; PAG, periaquaductal grey; pBF, posterior basal forebrain; PCRtA, parvocellular reticular nucleus Alpha part; pH, posterior hypothalamus; PMnR, paramedian nucleus; PnO_PnC, pontine reticular nucleus, oral and caudal parts; PTg, pedunculopontine nucleus; Pul, pulvinar; RMg, raphe magnus; RN, red nucleus; ROb, raphe obscurus; RPa, raphe pallidus; Sal/VA, salience / visual attention network; SC, superior colliculus; SCh, suprachiasmatic hypothalamic nucleus; SD, standard deviation; SM, somatomotor network; sMRt, superior medullary reticular formation; SN, substantia nigra; SN1, substantia nigra, subregion 1, compatible with reticulata; SN2, substantia nigra, subregion 2, compatible with comptacta; SO, supraoptic hypothalamic nucleus; SOC, superior olivary complex; SubC, subcoeruleus; SUVR, standard uptake value ratio; TM, tuberomammillary nucleus; VA, ventral anterior nucleus; Ve, vestibular nuclei complex; Vis, visual network; VLa, anterior part of ventral lateral nucleus; VLp, posterior part of the ventral lateral nucleus; VM, ventromedial hypothalamic nucleus; VPL, ventral posterolateral nucleus; and VSM, viscero-sensory-motor nuclei complex.

caudate nucleus from the data, the correlations changed from $r_s = 0.80$, $p = 0.007$ (panel a) to $r_s = 0.73$, $p = 0.031$; and from $r_s = 0.68$, $p = 0.035$ (panel b) to $r_s = 0.56$, $p = 0.12$.

Overall, the brain-wide spatial distribution of [^{18}F]FEOBV PET signal visually aligned to that of *SLC18A3* mRNA expression in the brain (Fig. 6). Spearman's rank correlations of [^{18}F]FEOBV PET distribution to regional expression of relevant genes are presented in Fig. 7. The regional uptake of [^{18}F]FEOBV PET correlated positively with log2 mRNA expression levels of all three cholinergic genes, but also with expression levels of one non-cholinergic control gene (*SLC18A2*).

3.4. Associations of regional [^{18}F]FEOBV PET signal with age and smoking status

Age did not correlate with [^{18}F]FEOBV PET binding in any region of interest. There were also no differences in tracer uptake comparing non-

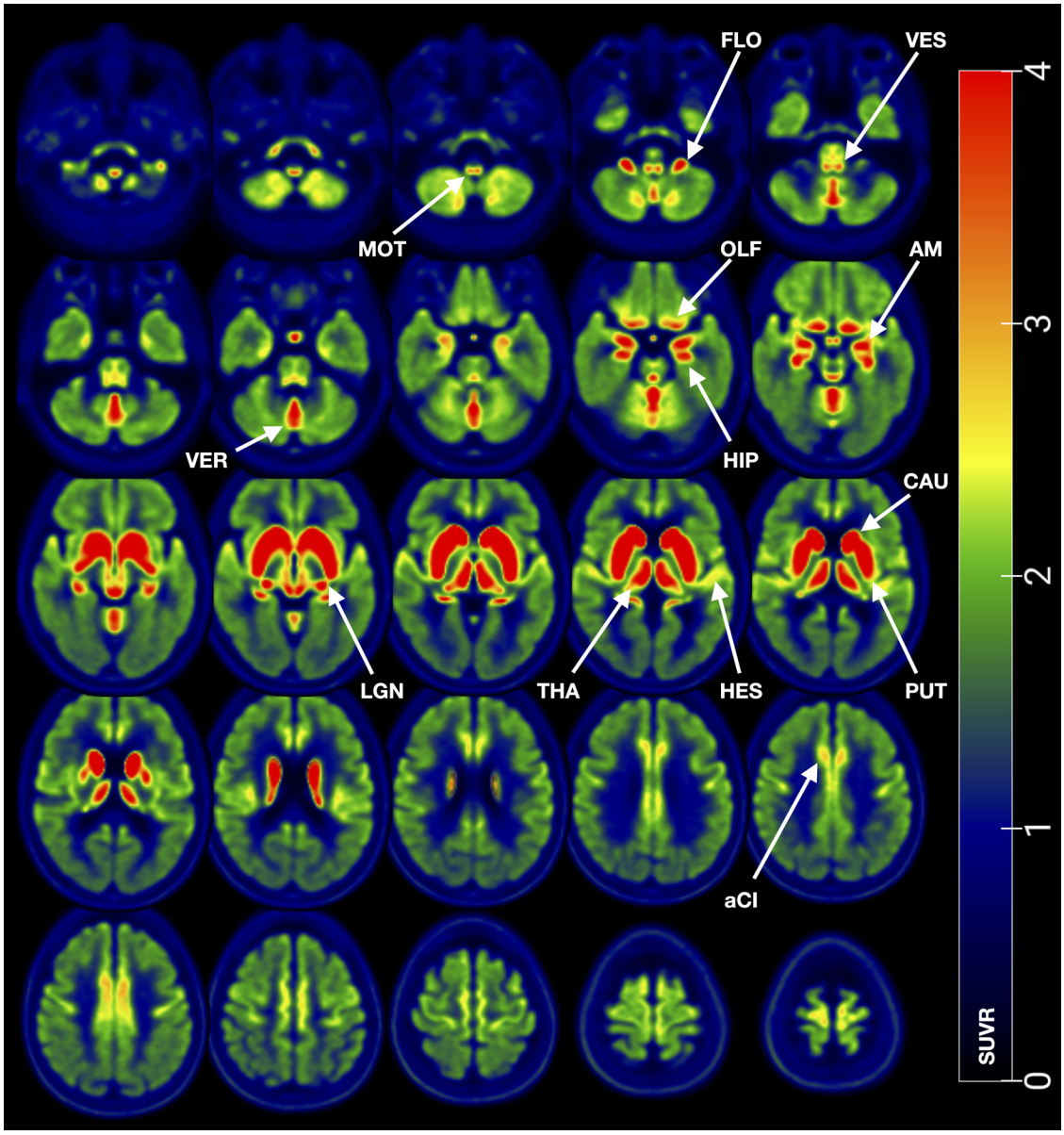

Fig. 1. Averaged axial slices of healthy elderly human brains imaged with [^{18}F]FEOBV PET. The [^{18}F]FEOBV PET image volumes are displayed in a mosaic of axial slices from the obex of the medulla oblongata to the vertex cranii. aCI, anterior cingulate; AM, amygdala; CAU, caudate; HIP, hippocampus; HES, Heschl's gyrus; LGN, lateral geniculate nucleus; MOT, dorsal motor nucleus of the vagus and hypoglossus nucleus; OLF, olfactory cortex; PUT, putamen; THA, thalamus; VER, vermis; VES, vestibular nucleus complex. Red colour indicates SUVR of 4 or higher.

smokers to current or previous smokers. Voxel-wise analyses yielded no significant effects at a threshold of $p < .05$, FDR corrected, nor when using a more lenient threshold of $p < .001$, uncorrected.

4. Discussion

This study presents the *in vivo* visualization and quantification of cortical and subcortical cholinergic uptake in the healthy aged human brain using [^{18}F]FEOBV PET. The distribution of [^{18}F]FEOBV PET aligns with histological evidence from post-mortem studies and with regional expression of cholinergic genes. There is a distinct and heterogenous cholinergic innervation of the cerebral cortex, brainstem, thalamus, hypothalamus, and cerebellum. The [^{18}F]FEOBV PET signal is considerably and consistently higher amongst subcortical structures compared to the cerebral cortex. There is a marked heterogeneity in signal within subcortical structures. Also, within the cerebral cortex there are clear regional differences.

The first [^{123}I]IBVM study in humans described the uptake in the striatum, thalamus, cortex, hippocampus, pons, and cerebellum (Kuhl et al., 1994). Later, the first [^{18}F]FEOBV PET study in healthy humans quantified the distribution in the same areas and also in the amygdala (Petrou et al., 2014). More recently, Albin et al. quantified the uptake of [^{18}F]FEOBV PET in the flocculus, putamen and caudate, and in the lateral geniculate nucleus of the thalamus, dividing the remaining thalamus into octants. The authors further parcellated the cortical distribution of tracer and quantified the uptake in the raphe nuclei and substantia nigra (Albin et al., 2018). A recent [^{18}F]FEOBV PET study used voxel-based analysis to study changes related to age, but did not report on the regional distribution of tracer (Kanel et al., 2022). As such, the present study represents an advancement in the continued efforts to delineate the spatial topography of the human cholinergic system *in vivo*.

Albin et al. used [^{18}F]FEOBV PET to describe the topography of cholinergic terminals in 29 subjects with a mean age of 47 years. In summary, they found high [^{18}F]FEOBV PET signal in the striatum; in-

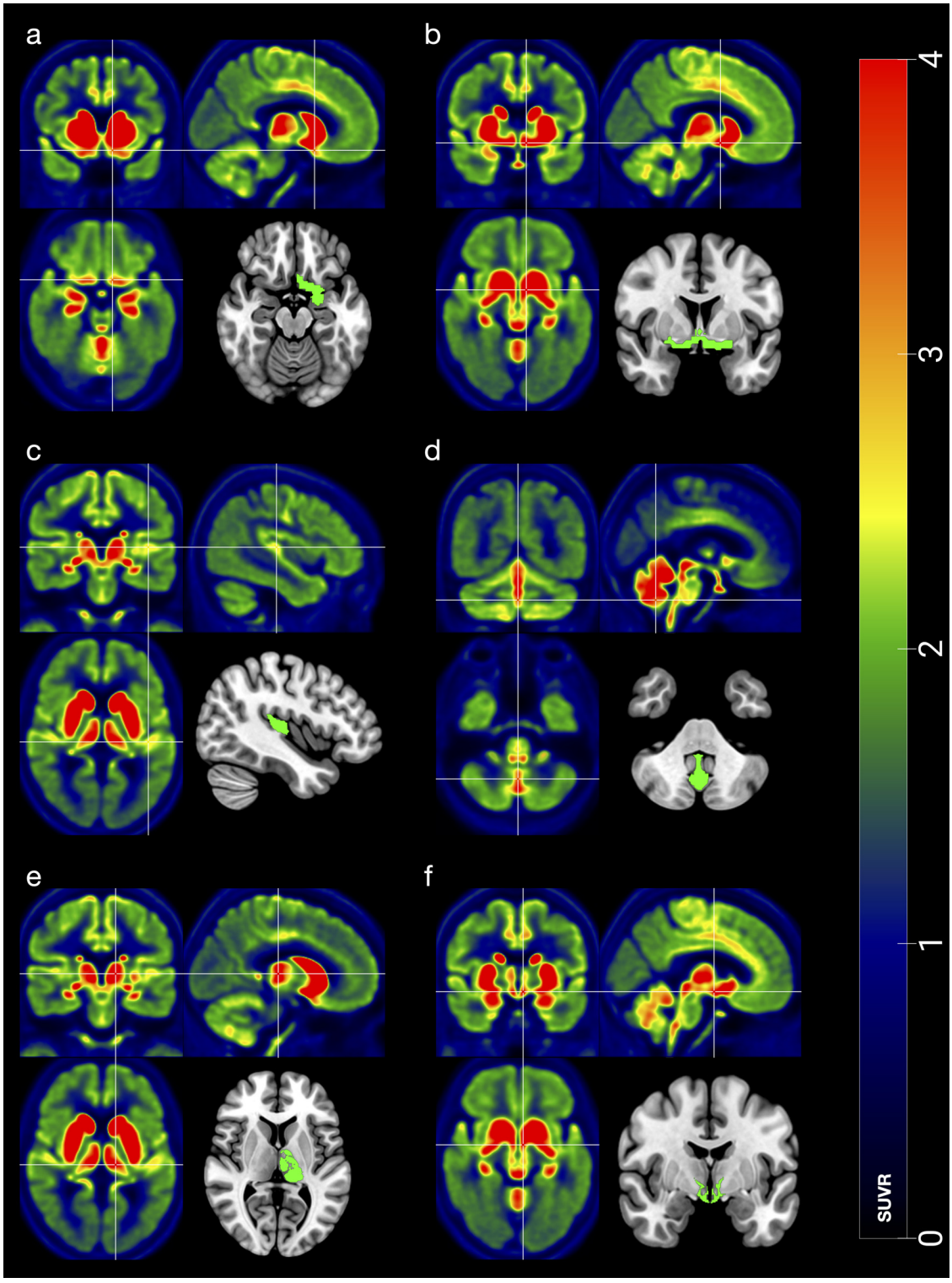

Fig. 2. Multi-planar view of selected regions of interest in healthy elderly human brains visualized with [^{18}F]FEOBV PET. Selected regions are presented as atlas superimposed on MNI templates with corresponding multi planar images generated from [^{18}F]FEOBV PET averages of healthy elderly human brains. Cross hairs indicate location of (a) olfactory cortex, (b) basal forebrain, (c) Heschl's gyrus, (d) vermis, (e) thalamus, and (f) hypothalamus. Red colour indicates SUVR of 4 or higher.

termediate in the amygdala, hippocampal formation, thalamus, rostral brainstem, and some cerebellar structures; and lower in other regions (Albin et al., 2018). Overall, we found a highly similar spatial distribution of [^{18}F]FEOBV PET. As our cohort had a mean age of 74 years, and some studies have shown an age-related decline in available VAChT protein, we would have expected to see somewhat lower levels of uptake (Albin et al., 2018; Kanel et al., 2022; Kuhl et al., 1996). Surprisingly, we found comparable magnitudes of mean regional uptake. This could be explained by our use of PET images with higher spatial resolution, which leads to higher SUV measurements in small structures.

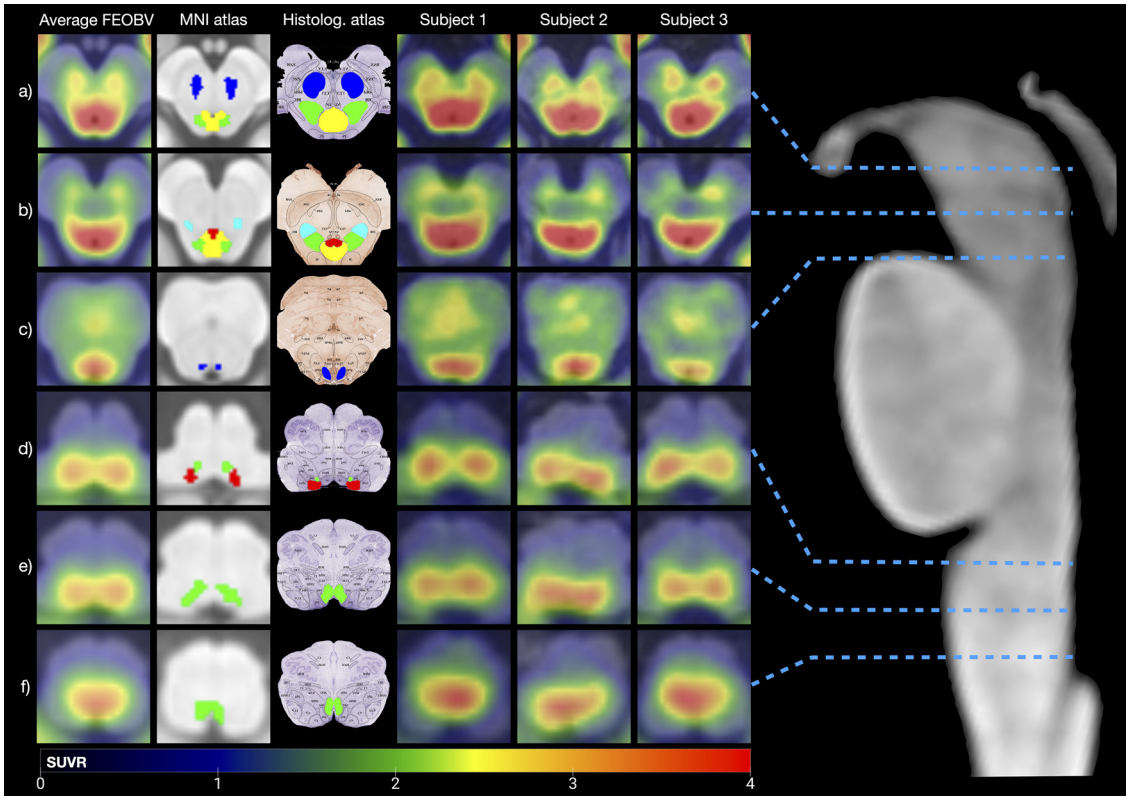

Fig. 3. Axial slices from [^{18}F]FEOBV PET images of healthy elderly human brainstems. The first column shows axial brainstem sections of an average image generated from 20 healthy elderly subjects superimposed on the MNI-template. The second column shows the same sections of the high-resolution structural MNI space template with atlas from the Brainstem Navigator toolkit superimposed. The third column depicts corresponding axial sections adapted from a histological atlas stained with ChAT and Lyxol Fast Blue (rows 2 and 3) or Cresyl Violet and Lyxol Fast Blue (remaining) (Coulombe et al., 2021). Corresponding nuclei in columns 2 and 3 have been marked with matching colours. Columns four through six present the corresponding axial sections of three individual PET scans superimposed on T1-weighted MRI images. Row (a) is rostral mesencephalon, CnF (cuneiform nucleus, green), PAG (periaquaductorial grey substance, yellow), RN (ruber nucleus, dark blue). Row (b) is mid-level mesencephalon, PTg (pedunculopontine nucleus, light blue), CnF (green), (dorsal raphe, red), PAG (yellow). Row (c) is the pontomesencephalic junction, LDTg_CGPn (laterodorsal tegmental nucleus and central grey of the rhombencephalon, dark blue). Row (d) is rostral medulla, Ve (vestibular nuclei complex, red), VSM (viscero-sensory-motor nuclei complex, green). Row (e) is mid-level medulla, and row (f) is caudal medulla, both depicting the VSM (green). Red colour indicates SUVR of 4 or higher. All images are angled perpendicular to the pontomesencephalic junction to match the histological atlas.

SLC18A3 mRNA expression and [^{18}F]FEOBV PET distribution correlated positively within the brain (Fig. 7, panel a). This finding further corroborates the validity of [^{18}F]FEOBV PET as a tool to study cholinergic terminals *in vivo*. There were also positive correlations with the genetic expression of choline acetyltransferase and acetylcholinesterase (Fig. 7, panels b and c). In rats, the expression of mRNA encoding VAChT is consistent with the distribution of cholinergic neurons in the central and peripheral nervous system (Schäfer et al., 1994). To our knowledge, the correlation of VAChT mRNA to VAChT protein has never been studied in post-mortem human tissue.

The spatial distribution of [^{18}F]FEOBV PET signal in the brain was generally consistent with that of *SLC18A3* mRNA expression, as shown in Fig. 6. However, there were some visible differences between the distributions at the subregional level, such as within subnuclei of the thalamus. One possible explanation for these subcortical differences may be that the mRNA expression data, which was derived from microarray measurements, has less spatial detail in subcortical structures compared to cortical structures (Hawrylycz et al., 2012). This can be seen in the brainstem and cerebellum, where the mRNA map has limited resolution. There were also misalignments between the two distributions in some cortical areas, such as in the parietal region, which may be due to sample variation in the microarray data, which was derived from six non-elderly brain donors and based on predictions in areas without samples (Gryglewski et al., 2018).

Unexpectedly, we also found a positive correlation to the genetic expression of *SLC18A2*, the gene for the vesicular monoamine transporter 2 (VMAT2). A previous study investigated the distribution of VMAT2 in healthy elderly human brains using [^{18}F]DTBZ PET (Lin et al., 2013). They found high uptake in the striatum, followed by the hypothalamus, raphe nuclei, hippocampus, and amygdala. Other subcortical regions including the thalamus had moderate uptake. The uptake was slightly lower in the cerebellum, and lowest in the cerebral cortex where binding was higher in frontal and temporal regions compared to parietal and occipital. In summary, the cerebral distribution of [^{18}F]DTBZ PET shows considerable similarity to the distribution of [^{18}F]FEOBV PET, which likely explains why the genetic expression of *SLC18A2* correlated with our regional distribution of [^{18}F]FEOBV PET uptake.

The *in vivo* [^{18}F]FEOBV PET signal showed robust spatial correlations with histological estimates of cholinergic system distribution across several histological studies differing in sample sizes, numbers of assessed regions, employed cholinergic marker, and other methodological details (Fig. 5). Notably, DeKosky et al.'s study of ChAT enzymatic activity used a sample size and demographic composition similar to ours (Fig. 5, panel c) (DeKosky et al., 2002). This finding adds credibility to [^{18}F]FEOBV as a marker of cholinergic neurons, and its applicability in studies investigating subregions/nuclei of subcortical structures. Also, the correlation with post-mortem data serves as a validation of the use of MNI-space atlases for measuring the heterogeneous uptake of [^{18}F]FEOBV in subcortical structures such as the thalamus and hypothalamus.

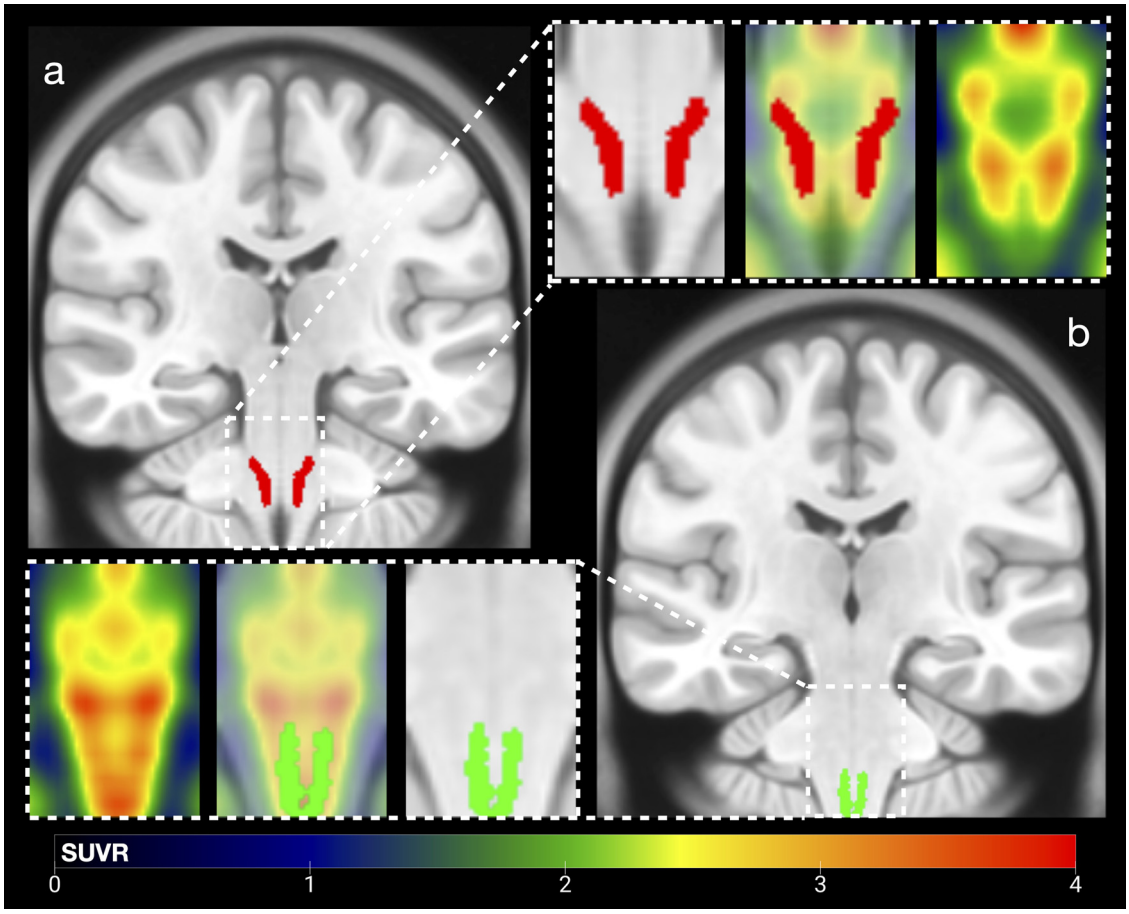

Fig. 4. Distribution of [^{18}F]FEOBV PET in the medulla oblongata and lower pons. Atlas from the Brainstem Navigator toolkit are superimposed on an average [^{18}F]FEOBV PET of 20 healthy controls overlayed on a coronal section of the MNI space template. The vestibular nuclei complex (a, red) including the medial vestibular nucleus, and the viscero-sensory-motor nuclei complex (b, green) including the dorsal motor nucleus of the vagus and hypoglossus are displayed. All images angled perpendicular to the pontomesencephalic junction. Red colour indicates SUVR of 4 or higher.

All areas of the central nervous system had an uptake above that seen in regions with mainly unspecific binding. This reflects that most areas of the human CNS receive cholinergic innervation, analogous to other mammals (Woolf, 1991). Studies using tracers that bind to nicotinic acetylcholine receptors have found that uptake is generally higher in subcortical structures compared to cortical areas, with the notable exception of the striatum (Kimes et al., 2008; Ellis et al., 2009). When compared to our findings, this suggests that the ratio of nicotinic receptors to cholinergic neurons is low in the striatum, which may indicate important differences in the cholinergic system of the striatum compared to other regions. On the other hand, studies using tracers that target muscarinic acetylcholine receptors find high uptake in cortical areas compared to subcortical structures (Zubieta et al., 2001; Yoshida et al., 1998). This underlines the significance of cortical cholinergic signalling, despite the relatively modest cortical [^{18}F]FEOBV PET uptake described in this study.

In the medulla, there was a distinct signal, which corresponded reasonably to the location of the DMV/XII and vestibular nuclei complex (Fig. 4). Studies using immunohistochemical techniques show that the DMV, XII, and MVN stain for ChAT (Oda, 1999; Woolf, 1991; Barmack et al., 1992b). This suggests that the medullary uptake of [^{18}F]FEOBV PET at least partly originates from the DMV, XII, and MVN. The DMV may harbour pathology in very early stages of Lewy body disorders such as Parkinson's disease and dementia with Lewy bodies (Del Tredici et al., 2002). Accordingly, a very recent [^{18}F]FEOBV PET study found that patients with REM Sleep behaviour Disorder, a known precursor to Parkinson's disease and dementia with Lewy bodies, exhibit cholinergic changes in the medulla oblongata and other brainstem regions (Bedard et al., 2019). We also observed a distinct [^{18}F]FEOBV uptake in the olfactory cortex (Fig. 2, panel a). Hyposmia is a common prodromal feature of Parkinson's disease and dementia with Lewy bodies and has been linked to cholinergic denervation in a previous cholinergic PET study (Fereshtehnejad et al., 2019; Bohnen et al., 2010). As such, improving the methods for *in vivo* molecular imaging of cholinergic structures may be important to advance our understanding of early-stage Lewy body disease.

The thalamic uptake showed a characteristic regional distribution of signal that correlated with findings from human post-mortem immunohistochemical staining for choline acetyltransferase (ChAT) (Fig. 5, panel f) (Heckers et al., 1992). In our data, the centromedian nucleus (CM) had highest uptake amongst the thalamic nuclei (Table 1). Interestingly, the CM is being considered a potential target for deep-brain stimulation for a range of disorders including Tourette syndrome, intractable pain, Parkinson's disease, and in restoring consciousness (Ilyas et al., 2019). To our knowledge, no other cholinergic molecular studies have parcellated the thalamic uptake using stereotactic maps.

In the cerebral cortex, we found a high salience network signal. This distribution aligned well with a previous cholinergic PET study specifically focused on neocortical signal distribution (Picard et al., 2013). Also, an rs-fMRI study found the limbic, salience, and auditory networks

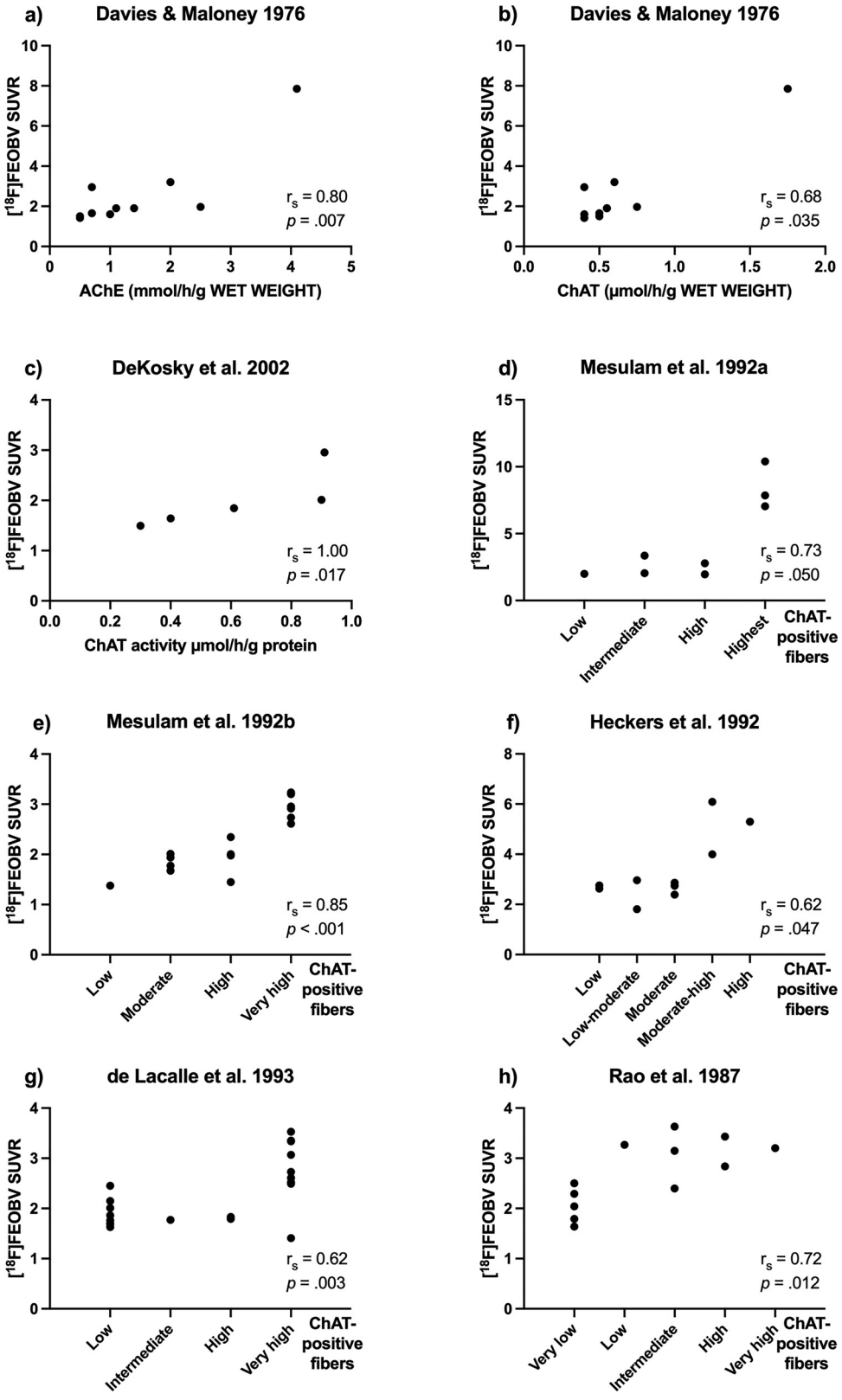

Fig. 5. Correlations of [^{18}F]FEOBV PET distribution in the brain to published data from histologic material. Twenty [^{18}F]FEOBV PET images of healthy elderly subjects were transferred to MNI-space and averaged. Stereotactic atlases were superimposed to define regions of interest and extract SUVR values. Cortical and subcortical regions were defined using the Jülich Brain cytoarchitectonic atlas; Hammers atlas; atlas of thalamic nuclei; atlas from the Brainstem Navigator toolkit; and atlas of hypothalamic structures. The panels present Spearman's rank correlations of regional [^{18}F]FEOBV PET SUVR to enzymatic activities and immunohistochemical staining: AChE (a) and ChAT (b) enzymatic activity in the hippocampus, amygdala, parietal cortex, sensory cortex, occipital cortex, frontal cortex, caudate, substantia nigra, mid-brain, pons (Davies and Maloney, 1976); ChAT enzymatic activity in the hippocampus, inferior parietal, superior frontal, anterior cingulate, superior temporal (c) (DeKosky et al., 2002); immunohistochemical ChAT fibre staining intensity in caudate, putamen, accumbens, red nucleus, subthalamic nucleus, globus pallidus, ventral tegmental area, substantia nigra pars compacta (d) (Mesulam et al., 1992); entorhinal region, amygdala, amygdala subregions (laterobasal, centromedial, superficial), hippocampus, hippocampal subregions (CA4, CA3, CA2, CA1), primary visual cortex, primary auditory cortex, somatosensory cortex, primary motor cortex, premotor area, cingulate gyrus (e) (Mesulam et al., 1992); thalamic nuclei (centre median, mediodorsal, anteroventral, ventral posterior lateral, lateral geniculate, medial geniculate, ventral anterior, ventral lateral anterior, ventral lateral posterior, pulvinar, and habenula) (f) (Heckers et al., 1992); cerebellum (g) (de Lacalle et al., 1993); and hypothalamus (h) (Rao et al., 1987). Panels (a) - (g) are based on human tissue and (h) is rat. Data on enzymatic activities are reported as continuous data, and immunohistochemical staining intensities on ordinal, semi-quantitative scales.

to have the highest connectivity with the nucleus basalis of Meynert (NBM) (Fritz et al., 2019). This is interesting, as the NBM harbors the cholinergic cell bodies innervating the cerebral cortex. This connectivity perfectly aligns with the cortical networks with highest [^{18}F]FEOBV PET signal in our study (Table 1).

AChE staining in human post-mortem tissue has demonstrated a high concentration in the primary auditory cortex, and markedly lower concentration in nearby associated cortical areas (Hutsler and Gazzaniga, 1996). These findings match the distribution of [^{18}F]FEOBV PET in our study (Fig. 2, panel c). As VAChT is specific to cholinergic nerves,

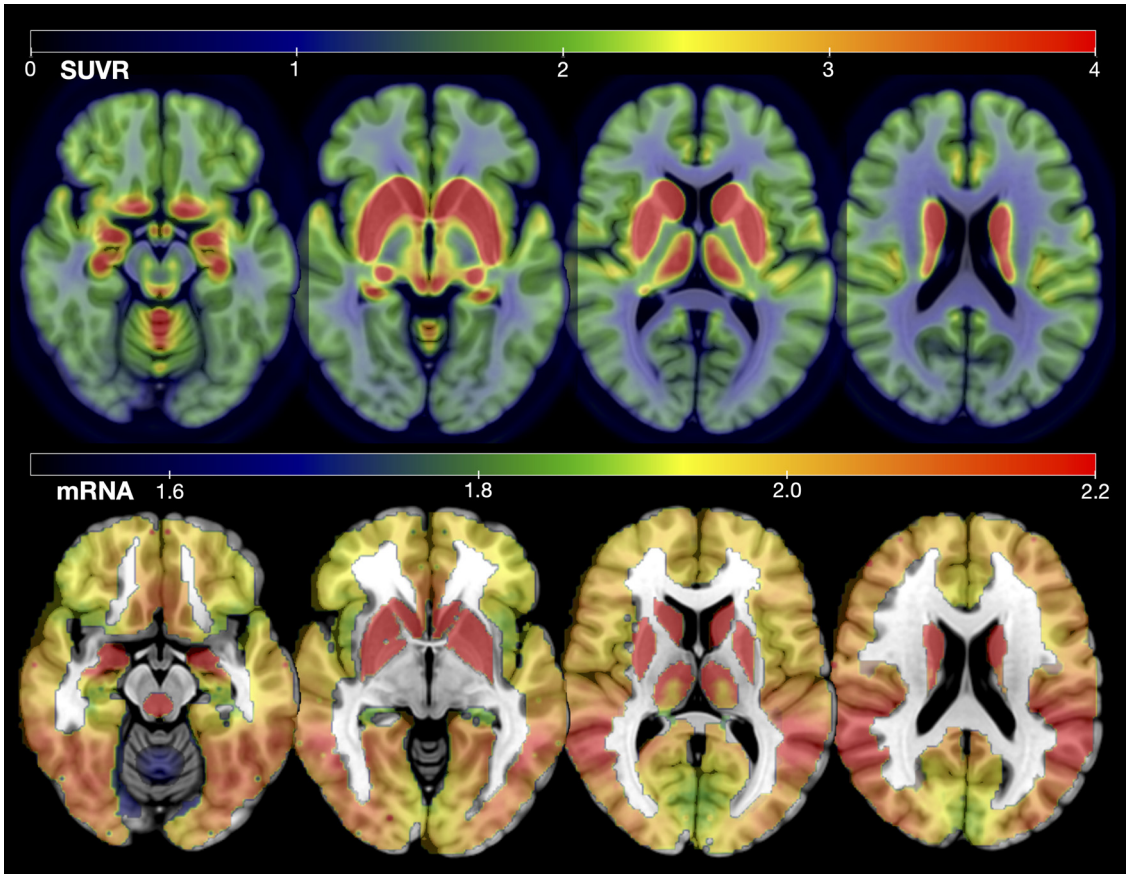

Fig. 6. Predicted spatial distribution of *SLC18A3* (VAChT gene) messenger ribonucleic acid (mRNA) expression levels compared to [^{18}F]FEOBV PET. The top row presents four axial slices from an average [^{18}F]FEOBV PET image generated from 20 healthy elderly subjects superimposed on the MNI space template scaled to an SUVR of 4. The bottom row shows the distribution of *SLC18A3* mRNA expression levels on the same four axial slices scaled to a value of 1.51–2.20 of log2 mRNA expression intensity.

and AChE is also located in non-cholinergic neurons, our findings contribute evidence to a particularly high cholinergic innervation of the primary auditory cortex.

In the cerebellum we found that the uptake was most pronounced in the vermis and flocculonodular lobe, as previously reported (Albin et al., 2018). Studies using PET tracers targeting AChE have shown distributions of tracer which partly overlap with that of [^{18}F]FEOBV. Most notably, the cerebellar cortex seems to contain high levels of AChE. In contrast, [^{18}F]FEOBV delineates several high-binding structures more clearly, including Heschl's gyrus, thalamic subnuclei, brainstem nuclei, and limbic regions (Shinotoh et al., 2003; Kuhl et al., 1999; Okamura et al., 2008). These discrepancies are notable because they suggest significant contributions of non-cholinergic neurons to the AChE-PET signal, and that tracers targeting VAChT are more specific markers of the presynaptic aspects of the cholinergic system.

The hypothalamic distribution of [^{18}F]FEOBV PET in elderly humans correlated with the immunohistochemical ChAT staining in rats (Fig. 5, panel h) (Rao et al., 1987). The distribution was also in agreement with studies staining for VAChT mRNA and protein in rats, and ChAT in monkey and human tissue (Tago et al., 1987; Ichikawa et al., 1997). In our data, there was high uptake in hypothalamic structures relevant for thermoregulation, defensive behaviour, food intake, sexual behaviour, thirst, and sleep-wake cycle. To our knowledge, the present study is the first human *in vivo* assessment of the cholinergic hypothalamus. In general, the implications of hypothalamic cholinergic innervation have received very little attention so far.

This study examined the cholinergic system in cognitively healthy elderly individuals. While many research studies on cholinergic imaging have focused on neurodegenerative disorders such as Parkinson's and Alzheimer's disease, which are common in the elderly population, it is also important to understand the cholinergic system in elderly people without these diseases. By studying cognitively intact elderly individuals, we can better understand the changes in the cholinergic system due to normal ageing, as opposed to those caused by disease. This information can be useful when comparing elderly individuals with neurodegenerative diseases to a control group of cognitively healthy elderly individuals. A previous [^{18}F]FEOBV PET study found a correlation between age and regional binding that we could not replicate in this cohort (Albin et al., 2018). Another study used voxel-wise analysis and reported several clusters of age-related reductions in binding that also survived multiple comparison correction using a cluster-level family-wise error rate of $p<.05$ (Kanel et al., 2022). This discrepancy between our results and these previous studies may not be surprising, as both cohorts had a wider age span (20 to 80 years) compared to our cohort (65 to 86 years).

Prior studies have not examined the effect of smoking on VAChT or ChAT in human brain tissue but have shown that smoking affects other aspects of the cholinergic system (Brody et al., 2011). Prenatal smoke exposure in rodents may alter ChAT and VAChT expression, and human studies suggest smoking may alter ChAT expression in non-neuronal tissue (Mao et al., 2008; Profita et al., 2009). As such, the effects of smoking on [^{18}F]FEOBV PET uptake in the human brain is an important but largely unexplored topic in the field. In our study, we found no differ-

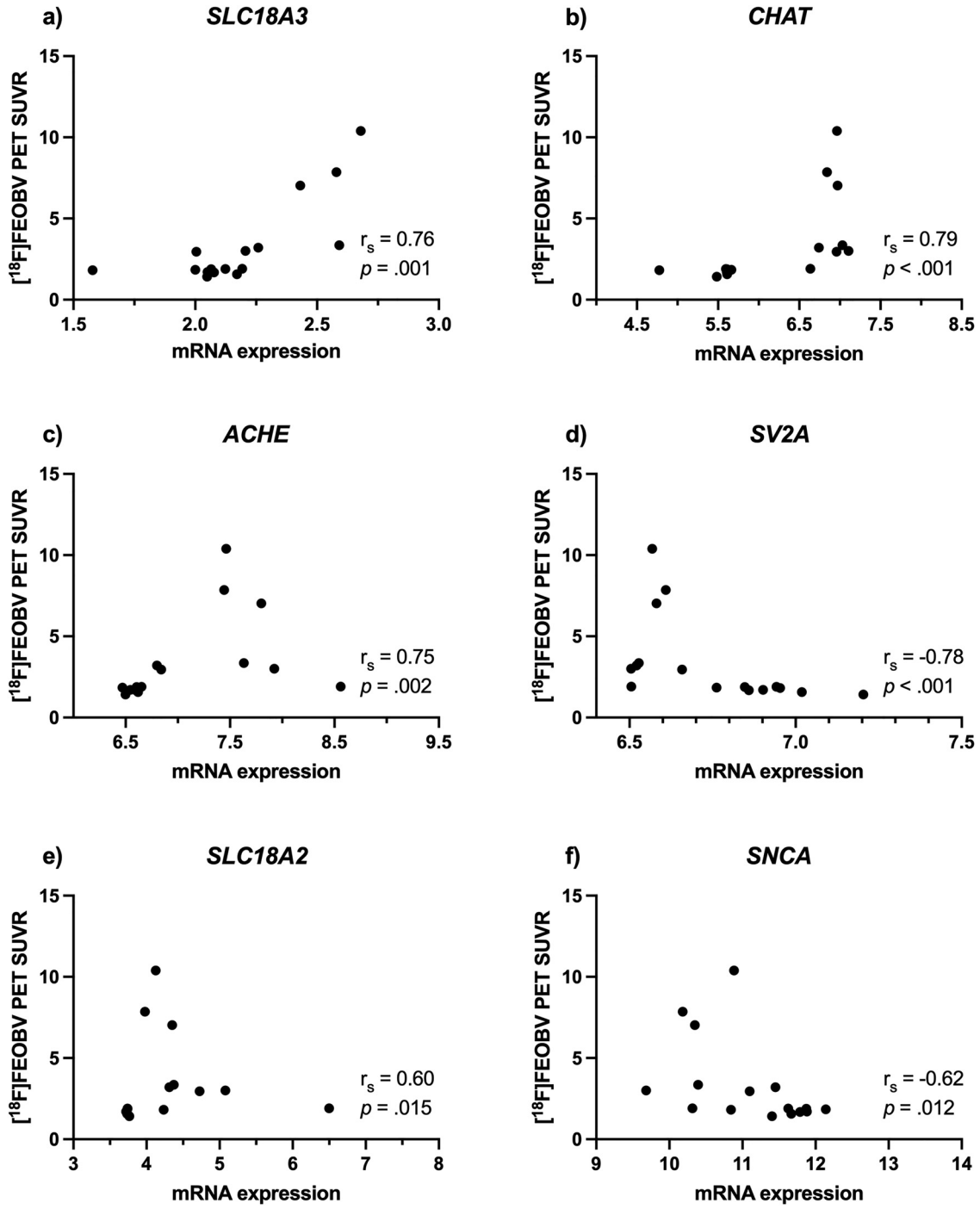

Fig. 7. Correlations of [18F]FEOBV PET distribution to messenger ribonucleic acid (mRNA) log2 expression of three cholinergic and three non-cholinergic genes. Correlations are calculated across 16 cortical and subcortical regions. The cortical regions were the somatomotor network, salience/visual attention network, limbic network, default mode network, control network, dorsal attention network, and visual network – all derived from Yeo's atlas of cortical networks. The subcortical regions were the hippocampus, amygdala, caudate, accumbens, putamen, pallidum, thalamus, cerebellum, and brainstem – all derived from the Hammers atlas. Regional uptake of [18F]FEOBV PET is plotted against regional expression levels of *SLC18A3*, the gene for the vesicular acetylcholine transporter (VAChT) (a); *CHAT*, the gene for choline acetyltransferase (b); *ACHE*, the gene for acetylcholinesterase (c); *SV2A*, the gene for synaptic vesicle glycoprotein 2A (d); *SLC18A2*, the gene for the vesicle monoamine transporter 2 (VMAT2) (e); and *SNCA*, the gene for alpha synuclein (f).

ences in tracer uptake comparing non-smokers to current or previous smokers.

[18F]FEOBV binds to VAChT which is located mainly in cholinergic terminals, and to a lesser extend in cholinergic cell bodies. This means that the distribution of tracer reflects both cholinergic structures and non-cholinergic structures that receive cholinergic innervation. For example, the cortex displays considerable tracer uptake, but has no intrinsic cholinergic cell bodies. Also, we cannot know if the signal from regions that are known to harbour cholinergic cell bodies, such as the motor nuclei of the brainstem, reflect VAChT located in the cell bodies of the nuclei or cholinergic afferent terminals. As such, the uptake of tracer in the basal forebrain probably represents both the cholinergic

cell bodies of the basal forebrain and the cholinergic brainstem afferents terminating on the basal forebrain.

In conclusion, this study presents the *in vivo* distribution of cholinergic neurons and in particular their terminals in the aged human brain. The spatial signal distribution amongst relevant subcortical structures is comparable to that of human post-mortem histological staining studies. This suggests that [^{18}F]FEOBV PET can also be used to explore the cholinergic innervation of areas in the human brain that have not been fully explored in human post-mortem studies, thereby contributing to our general knowledge of the anatomy of the cholinergic system in general. Also, the regional distribution of [^{18}F]FEOBV PET correlates with the mRNA expression of *SLC18A3*, the gene encoding VAChT, which further strengthens the validity of [^{18}F]FEOBV PET as a tool to study the brain's cholinergic system. Finally, and perhaps most interestingly, the study presents details about the cholinergic system in areas that have not yet been studied neither *in vivo* nor in post-mortem human studies, such as the hypothalamus. The findings may have implications for studies aiming to understand the role of the cholinergic system in normal physiology, but also in neuromuscular, autonomic, and neurodegenerative disorders.

Funding sources

MJG is supported by the "Miguel Servet" program [CP19/00031] and a research grant [PI20/00613] of the Instituto de Salud Carlos III-Fondo Europeo de Desarrollo Regional (ISCIII-FEDER). PB is supported by grants from the Lundbeck foundation (R-359–2020–2533) and Michael J Fox Foundation (MJFF-022856). The funding sources were not involved in the conceptualization, collection, analysis, or interpretation of data; in writing of the report; or the decision to submit the article for publication.

Declarations of Competing Interest

None.

Credit authorship contribution statement

Niels Okkels: Conceptualization, Methodology, Validation, Formal analysis, Investigation, Writing – original draft, Writing – review & editing, Visualization. **Jacob Horsager:** Conceptualization, Methodology, Investigation. **Miguel A. Labrador-Espinosa:** Software, Formal analysis, Supervision. **Frederik O. Hansen:** Investigation. **Katrine B. Andersen:** Software, Formal analysis, Visualization. **Mie Kristine Just:** Methodology, Visualization. **Tatyana D. Fedorova:** Investigation. **Casper Skjærbæk:** Investigation. **Ole L. Munk:** Methodology, Software. **Kim V. Hansen:** Software, Resources. **Hanne Gottrup:** Supervision. **Allan K. Hansen:** Conceptualization, Formal analysis, Supervision. **Michel J. Grothe:** Conceptualization, Methodology, Software, Validation, Formal analysis, Writing – review & editing, Supervision. **Per Borghammer:** Conceptualization, Methodology, Formal analysis, Resources, Writing – review & editing, Supervision, Project administration, Funding acquisition.

Data availability

Data sharing would require a formal data sharing agreement approved by the relevant local ethics committees.

Supplementary materials

Supplementary material associated with this article can be found, in the online version, at doi:10.1016/j.neuroimage.2023.119908.

References

Aghourian, M., Legault-Denis, C., Soucy, J.P., Rosa-Neto, P., Gauthier, S., Kostikov, A., et al., 2017. Quantification of brain cholinergic denervation in Alzheimer's disease using PET imaging with [(18)F]-FEOBV. Mol. Psychiatry 22 (11), 1531–1538.

Albin, R.L., Bohnen, N.I., Muller, M., Dauer, W.T., Sarter, M., Frey, K.A., et al., 2018. Regional vesicular acetylcholine transporter distribution in human brain: a [(18)F]fluoroethoxybenzovesamicol positron emission tomography study. J. Comp. Neurol. 526 (17), 2884–2897.

Amunts, K., Mohlberg, H., Bludau, S., Zilles, K., 2020. Julich-Brain: a 3D probabilistic atlas of the human brain's cytoarchitecture. Science 369 (6506), 988–992.

Ashburner, J., 2007. A fast diffeomorphic image registration algorithm. Neuroimage 38 (1), 95–113.

Barmack, N., Baughman, R., Eckenstein, F., 1992a. Cholinergic innervation of the cerebellum of rat, rabbit, cat, and monkey as revealed by choline acetyltransferase activity and immunohistochemistry. J. Comp. Neurol. 317 (3), 233–249.

Barmack, N., Baughman, R., Eckenstein, F., Shojaku, H., 1992b. Secondary vestibular cholinergic projection to the cerebellum of rabbit and rat as revealed by choline acetyltransferase immunohistochemistry, retrograde and orthograde tracers. J. Comp. Neurol. 317 (3), 250–270.

Bedard, M.-A., Aghourian, M., Legault-Denis, C., Postuma, R.B., Soucy, J.-P., Gagnon, J.-F., et al., 2019. Brain cholinergic alterations in idiopathic REM sleep behaviour disorder: a PET imaging study with 18F-FEOBV. Sleep Med. 58, 35–41.

Bianciardi, M., Strong, C., Toschi, N., Edlow, B.L., Fischl, B., Brown, E.N., et al., 2018. A probabilistic template of human mesopontine tegmental nuclei from *in vivo* 7T MRI. Neuroimage 170, 222–230.

Bohnen, N.I., Müller, M.L., Kotagal, V., Koeppe, R.A., Kilbourn, M.A., Albin, R.L., et al., 2010. Olfactory dysfunction, central cholinergic integrity and cognitive impairment in Parkinson's disease. Brain 133 (6), 1747–1754.

Brody, A.L., Mandelkern, M.A., London, E.D., Khan, A., Kozman, D., Costello, M.R., et al., 2011. Effect of secondhand smoke on occupancy of nicotinic acetylcholine receptors in brain. Arch. Gen. Psychiatry 68 (9), 953–960.

Coulombe, V., Saikali, S., Goetz, L., Takech, M.A., Philippe, E., Parent, A., et al., 2021. A topographic atlas of the human brainstem in the ponto-mesencephalic junction plane. Front. Neuroanat. 15, 627656.

Davies, P., Maloney, A., 1976. Selective loss of central cholinergic neurons in Alzheimer's disease. Lancet N. Am. Ed. 308 (8000), 1403.

de Lacalle, S., Hersh, L.B., Saper, C.B, 1993. Cholinergic innervation of the human cerebellum. J. Comp. Neurol. 328 (3), 364–376.

DeKosky, S.T., Ikonomovic, M.D., Styren, S.D., Beckett, L., Wisniewski, S., Bennett, D.A., et al., 2002. Upregulation of choline acetyltransferase activity in hippocampus and frontal cortex of elderly subjects with mild cognitive impairment. Ann. Neurol. 51 (2), 145–155 Official Journal of the American Neurological Association and the Child Neurology Society.

Del Tredici, K., Rüb, U., De Vos, R.A., Bohl, J.R., Braak, H., 2002. Where does Parkinson disease pathology begin in the brain? J. Neuropathol. Exp. Neurol. 61 (5), 413–426.

Diedrichsen, J., Balsters, J.H., Flavell, J., Cussans, E., Ramnani, N., 2009. A probabilistic MR atlas of the human cerebellum. Neuroimage 46 (1), 39–46.

Ellis, J.R., Nathan, P.J., Villemagne, V.L., Mulligan, R., Ellis, K., Tochon-Danguy, H., et al., 2009. The relationship between nicotinic receptors and cognitive functioning in healthy aging: an *in vivo* positron emission tomography (PET) study with 2-[18F] fluoro-A-85380. Synapse 63 (9), 752–763.

Fereshtehnejad, S.M., Yao, C., Pelletier, A., Montplaisir, J.Y., Gagnon, J.F., Postuma, R.B., 2019. Evolution of prodromal Parkinson's disease and dementia with Lewy bodies: a prospective study. Brain 142 (7), 2051–2067.

Fjaeldstad, A., Fernandes, H.M., Van Hartevelt, T.J., Gleesborg, C., Moller, A., Ovesen, T., et al., 2017. Brain fingerprints of olfaction: a novel structural method for assessing olfactory cortical networks in health and disease. Sci. Rep. 7, 42534.

Fritz, H.J., Ray, N., Dyrba, M., Sorg, C., Teipel, S., Grothe, M.J., 2019. The corticotopic organization of the human basal forebrain as revealed by regionally selective functional connectivity profiles. Hum. Brain Mapp. 40 (3), 868–878.

García-Gomar, M.G., Videnovic, A., Singh, K., Stauder, M., Lewis, L.D., Wald, L.L., et al., 2021. Disruption of brainstem structural connectivity in REM sleep behavior disorder using 7 tesla magnetic resonance imaging. Mov. Disord..

Gilmor, M.L., Nash, N.R., Roghani, A., Edwards, R.H., Yi, H., Hersch, S.M., et al., 1996. Expression of the putative vesicular acetylcholine transporter in rat brain and localization in cholinergic synaptic vesicles. J. Neurosci. 16 (7), 2179–2190.

Gryglewski, G., Seiger, R., James, G.M., Godbersen, G.M., Komorowski, A., Unterholzner, J., et al., 2018. Spatial analysis and high resolution mapping of the human whole-brain transcriptome for integrative analysis in neuroimaging. Neuroimage 176, 259–267.

Hammers, A., Allom, R., Koepp, M.J., Free, S.L., Myers, R., Lemieux, L., et al., 2003. Three-dimensional maximum probability atlas of the human brain, with particular reference to the temporal lobe. Hum. Brain Mapp. 19 (4), 224–247.

Hawrylycz, M.J., Lein, E.S., Guillozet-Bongaarts, A.L., Shen, E.H., Ng, L., Miller, J.A., et al., 2012. An anatomically comprehensive atlas of the adult human brain transcriptome. Nature 489 (7416), 391–399.

Heckers, S., Geula, C., Mesulam, M.M., 1992. Cholinergic innervation of the human thalamus: dual origin and differential nuclear distribution. J. Comp. Neurol. 325 (1), 68–82.

Hutsler, J.J., Gazzaniga, M.S., 1996. Acetylcholinesterase staining in human auditory and language cortices: regional variation of structural features. Cereb. Cortex 6 (2), 260–270.

Ichikawa, T., Ajiki, K., Matsuura, J., Misawa, H., 1997. Localization of two cholinergic markers, choline acetyltransferase and vesicular acetylcholine transporter in the cen-

tral nervous system of the rat: *in situ* hybridization histochemistry and immunohistochemistry. J. Chem. Neuroanat. 13 (1), 23–39.
Ilyas, A., Pizarro, D., Romeo, A.K., Riley, K.O., Pati, S., 2019. The centromedian nucleus: anatomy, physiology, and clinical implications. J. Clin. Neurosci. 63, 1–7.
Kanel, P., van der Zee, S., Sanchez-Catasus, C.A., Koeppe, R.A., Scott, P.J.H., van Laar, T., et al., 2022. Cerebral topography of vesicular cholinergic transporter changes in neurologically intact adults: a [18F]FEOBV PET study. Aging Brain 2.
Kimes, A.S., Chefer, S.I., Matochik, J.A., Contoreggi, C.S., Vaupel, D.B., Stein, E.A., et al., 2008. Quantification of nicotinic acetylcholine receptors in the human brain with PET: bolus plus infusion administration of 2-[18F] F-A85380. Neuroimage 39 (2), 717–727.
Kuhl, D.E., Koeppe, R.A., Fessler, J.A., Minoshima, S., Ackermann, R.J., Carey, J.E., et al., 1994. *In vivo* mapping of cholinergic neurons in the human brain using SPECT and IBVM. J. Nucl. Med. 35 (3), 405–410.
Kuhl, D.E., Minoshima, S., Fessler, J.A., Ficaro, E.P., Wieland, D.M., Koeppe, R.A., et al., 1996. *In vivo* mapping of cholinergic terminals in normal aging, Alzheimer's disease, and Parkinson's disease. Ann. Neurol. 40 (3), 399–410 Official Journal of the American Neurological Association and the Child Neurology Society.
Kuhl, D., Koeppe, R., Minoshima, S., Snyder, S., Ficaro, E., Foster, N., et al., 1999. *In vivo* mapping of cerebral acetylcholinesterase activity in aging and Alzheimer's disease. Neurology 52 (4), 691.
Lin, K.J., Weng, Y.H., Hsieh, C.J., Lin, W.Y., Wey, S.P., Kung, M.P., et al., 2013. Brain imaging of vesicular monoamine transporter type 2 in healthy aging subjects by 18F-FP-(+)-DTBZ PET. PLoS One 8 (9), e75952.
Mao, C., Yuan, X., Zhang, H., Lv, J., Guan, J., Miao, L., et al., 2008. The effect of prenatal nicotine on mRNA of central cholinergic markers and hematological parameters in rat fetuses. Int. J. Dev. Neurosci. 26 (5), 467–475.
Mesulam, M.M., Mash, D., Hersh, L., Bothwell, M., Geula, C., 1992a. Cholinergic innervation of the human striatum, globus pallidus, subthalamic nucleus, substantia nigra, and red nucleus. J. Comp. Neurol. 323 (2), 252–268.
Mesulam, M.M., Hersh, L.B., Mash, D.C., Geula, C., 1992b. Differential cholinergic innervation within functional subdivisions of the human cerebral cortex: a choline acetyltransferase study. J. Comp. Neurol. 318 (3), 316–328.
Neudorfer, C., Germann, J., Elias, G.J.B., Gramer, R., Boutet, A., Lozano, A.M., 2020. A high-resolution *in vivo* magnetic resonance imaging atlas of the human hypothalamic region. Sci. Data 7 (1), 305.
Oda, Y., 1999. Choline acetyltransferase: the structure, distribution and pathologic changes in the central nervous system. Pathol. Int. 49 (11), 921–937.
Oishi, K., Faria, A., Jiang, H., Li, X., Akhter, K., Zhang, J., et al., 2009. Atlas-based whole brain white matter analysis using large deformation diffeomorphic metric mapping: application to normal elderly and Alzheimer's disease participants. Neuroimage 46 (2), 486–499.
Okamura, N., Funaki, Y., Tashiro, M., Kato, M., Ishikawa, Y., Maruyama, M., et al., 2008. *In vivo* visualization of donepezil binding in the brain of patients with Alzheimer's disease. Br. J. Clin. Pharmacol. 65 (4), 472–479.
Petrou, M., Frey, K.A., Kilbourn, M.R., Scott, P., Raffel, D.M., Bohnen, N.I., et al., 2014. *In vivo* imaging of human cholinergic nerve terminals with (-)-5-(18) F-fluoroethoxybenzovesamicol: biodistribution, dosimetry, and tracer kinetic analyses. J. Nucl. Med. 55 (3), 396–404.
Picard, F., Sadaghiani, S., Leroy, C., Courvoisier, D.S., Maroy, R., Bottlaender, M., 2013. High density of nicotinic receptors in the cingulo-insular network. Neuroimage 79, 42–51.
Profita, M., Bonanno, A., Siena, L., Bruno, A., Ferraro, M., Montalbano, A.M., et al., 2009. Smoke, choline acetyltransferase, muscarinic receptors, and fibroblast proliferation in chronic obstructive pulmonary disease. J. Pharmacol. Exp. Ther. 329 (2), 753–763.
Rao, Z., Yamano, M., Wanaka, A., Tatehata, T., Shiosaka, S., Tohyama, M., 1987. Distribution of cholinergic neurons and fibers in the hypothalamus of the rat using choline acetyltransferase as a marker. Neuroscience 20 (3), 923–934.
Rolls, E.T., Huang, C.C., Lin, C.P., Feng, J., Joliot, M., 2020. Automated anatomical labelling atlas 3. Neuroimage 206, 116189.
Saranathan, M., Iglehart, C., Monti, M., Tourdias, T., Rutt, B., 2021. *In vivo* high-resolution structural MRI-based atlas of human thalamic nuclei. Sci. Data 8 (1), 275.
Schäfer, M.K.-.H., Weihe, E., Varoqui, H., Eiden, L.E., Erickson, J.D., 1994. Distribution of the vesicular acetylcholine transporter (VAChT) in the central and peripheral nervous systems of the rat. J. Mol. Neurosci. 5 (1), 1–26.
Shinotoh, H., Fukushi, K., Nagatsuka, S., Tanaka, N., Aotsuka, A., Ota, T., et al., 2003. The amygdala and Alzheimer's disease: positron emission tomographic study of the cholinergic system. Ann. N. Y. Acad. Sci. 985 (1), 411–419.
Singh, K., Indovina, I., Augustinack, J.C., Nestor, K., Garcia-Gomar, M.G., Staab, J.P., et al., 2019. Probabilistic template of the lateral parabrachial nucleus, medial parabrachial nucleus, vestibular nuclei complex, and medullary viscero-sensory-motor nuclei complex in living humans from 7 tesla MRI. Front. Neurosci. 13, 1425.
Tago, H., McGeer, P., Bruce, G., Hersh, L, 1987. Distribution of choline acetyltransferase–containing neurons of the hypothalamus. Brain Res. 415 (1), 49–62.
Wolf, D., Bocchetta, M., Preboske, G.M., Boccardi, M., Grothe, M.J., 2017. Alzheimer's disease neuroimaging I. Reference standard space hippocampus labels according to the European Alzheimer's disease consortium-Alzheimer's disease neuroimaging initiative harmonized protocol: utility in automated volumetry. Alzheimers Dement 13 (8), 893–902.
Woolf, N.J., 1991. Cholinergic systems in mammalian brain and spinal cord. Prog. Neurobiol. 37 (6), 475–524.
Yeo, B.T., Krienen, F.M., Sepulcre, J., Sabuncu, M.R., Lashkari, D., Hollinshead, M., et al., 2011. The organization of the human cerebral cortex estimated by intrinsic functional connectivity. J. Neurophysiol..
Yoshida, T., Kuwabara, Y., Ichiya, Y., Sasaki, M., Fukumura, T., Ichimiya, A., et al., 1998. Cerebral muscarinic acetylcholinergic receptor measurement in Alzheimer's disease patients on11C-N-methyl-4-piperidyl benzilate—comparison with cerebral blood flow and cerebral glucose metabolism—. Ann. Nucl. Med. 12 (1), 35–42.
Zubieta, J.K., Koeppe, R.A., Frey, K.A., Kilbourn, M.R., Mangner, T.J., Foster, N.L., et al., 2001. Assessment of muscarinic receptor concentrations in aging and Alzheimer disease with [11C] NMPB and PET. Synapse 39 (4), 275–287.